Investigating the impurity of single carbon atom on the electronic transport of two side-closed $(6,6)$ single-walled boron nitride nanotubes

Ali Mohammad Yadollahi[1], Abolfazl Khodadadi[2], Masoumeh Firouzi[3], Mojtaba Yaghobi[1], Mohammad Reza Niazian[1*], Alireza Yekrangi Sendi[4]

[1]*Department of Physics, Ayatollah Amoli Branch, Islamic Azad University, Amol, Iran.*
[2]*Department of Physics, North Tehran Branch, Islamic Azad University, Tehran, Iran.*
[3]*Department of Physics, Kashan Branch, Islamic Azad University, Kashan, Iran.*
[4]*Department of Mechanical Engineering, Ramsar Branch, Islamic Azad University, Ramsar, Iran.*

*Corresponding author: m.reza.niazian@gmail.com

Abstract:

In this study, the impurity of a single carbon atom on the electronic properties of two side-closed $(6,6)$ single-walled boron nitride nanotubes ($(6,6)$ TSC-SWBNNTs) has been investigated in the right, left, and center of this nanotube using the Slater-Koster method and tight-binding approximation. The non-equilibrium Green's function approach has been used in this method. The figures of the transmission spectrum in the impurity state of the carbon atom in the right, left, and center of this nanotube were drawn at bias voltages of 0, 2.5, and 5 V and then compared with those of the DOS (density of states). In energy values where the peak of the transmission spectrum figure and the peak of the DOS exist simultaneously, the resonance state has occurred for the incoming electron. In addition, a new electron tunneling has occurred, and the current change can be observed as a jump and staircase state in the current figure according to the bias voltage. In addition, due to the effect of interference in the two ends of the nanotube and the reduction of the current in some values of the bias voltage, negative differential resistance can also be found, which can be employed as high-speed electronic switches.

1. Introduction

Carbon (C) nanostructures are widely used in various applications such as electronics, drug delivery, biomedicine, etc. due to their exceptional physical and chemical properties. However, due to their more excellent thermal and chemical stability and structural similarity with C nanomaterials, boron nitride (BN) nanostructures have attracted more attention than C nanostructures [1]. A considerable deal of attention has focused on the unique tubular structure and superior features of carbon nanotubes (CNTs) in different fields since their production by Iijima (1991) [2]. Essentially, BN nanotubes (BNNTs) are structurally similar to CNTs; generally, C atoms in a hexagonal plate are replaced alternatively by nitrogen (N)

and boron (B) atoms almost without a change in atomic spacing. BNNTs were theoretically predicted in 1994 and synthesized after a year by electric arc discharge [3, 4]. BNNTs, unlike CNTs, are electrical insulators with a band gap of about $5.5 - 6$ eV without dependency on the chirality, diameter, and number of nanotube walls [5]. In 2010, Wang *et al.* presented a brief review of the structure, theory, and physical features of BNNTs [6, 7]. However, the advantages of BNNTs over CNTs, including higher thermal conductivity, radiation protection, insulating properties, and non-toxicity, have led to the use of BNNTs in many fields like aerospace engineering, various biomedical applications, especially the possibility of the delivery of anti-cancer drugs, and tissue engineering. The main difference between
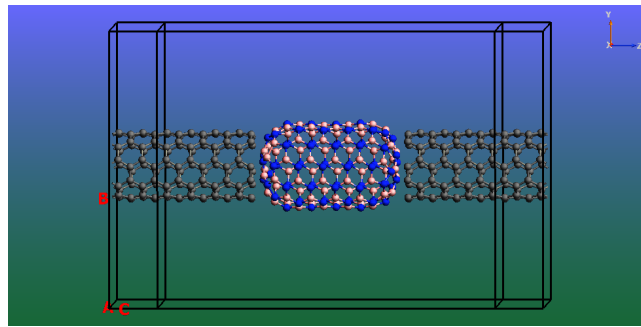
Figure 1. Tool created with two (5, 5) CNT electrodes on both sides and pure (6, 6) TSC-SWBNNT.

BNNTs and CNTs is the ionic property between the $B - N$ bonds, changing molecular orbital configuration [8]. Although nanomaterials without defects possess attractive physical features, in reality, defects are unavoidable, and experimentally BNNTs are usually not without defects [9–13]. Such defects are vacancies, Stone-Wales defects, and impurities with a considerable effect on the BNNTs properties [9, 10]. Research indicates that substituting a C element with B or N in the BNNT. Hence, the nanotube can be converted into an *n*-type or *p*-type semiconductor, as an electron is added by replacement of a *C* atom with B. However, a hole is made by replacement of a C atom with N [14, 15]. Considering the rapid development of nanofabrication methods, the amount of current can be estimated through molecule wires, which are connected to two electrodes [16, 17]. The rapid development of nanostructure techniques allows the measurement of the amount of current through two side-closed single-walled BNNTs (TSC-SWBNNTs) between two electrodes [18–22]. The transport properties of SWBNNTs are sensitive to defect configuration, so theoretical and experimental research is necessary to understand in detail the effect of defect arrangement on their electronic and transport properties. Therefore, the transport properties of the SWBNNTs are vital for fundamental research and potential applications of the systems in future nano-electronic devices. Yadollahi *et al.* [23] investigated the electronic transport properties of (6, 3) TSC-SWBNNT in the presence of C atom impurity. In this paper, the electronic properties of (6, 6) TSC-SWBNNTs were investigated in pure and impurity

states. The impurity state was considered by replacing the C atom with N and B atoms on the right, left, and center of (6, 6) TSC-SWBNNTs. These nanotubes have a different chirality than the nanotubes previously studied by Yadollahi *et al.* This difference is in the arrangement of atoms, length, and diameter of nanotubes and causes changes in their electronic properties. The figures of the transmission spectrum, the density of states (DOS), and bias current- voltage are drawn for each state. Further, the presence of negative differential resistance (NDR) has been investigated for the states as mentioned above.

2. Materials and methods

Due to the presence of many atoms in this structure, electronic properties have been studied with ATK's reliable simulation software. The basis of this is Python, which is robust and high-level software. Furthermore, Slater-Koster [24] and Force Field [25] methods, tight-binding approximation, and the NEGF approach have been used in this study). The two nanotube sides were closed via hexagons and pentagons of N and B atoms. The TSC-BNNTs axis is parallel to the *z*-axis. The mesh cut-off is 150 Rydbergs during the simulation process [26–28]. Brillouin zone was in $1 \times 1 \times 100$ dimensions with *K*-point [29–33]. The force tolerance of $0.01\,\text{eV}/A$ with the highest step of 500 has been employed to optimize the device. The CN (5, 5) with the repetition number of $1 \times 1 \times 4$ is utilized in the electrodes. Based on NEGF relations with bias voltage *V* and
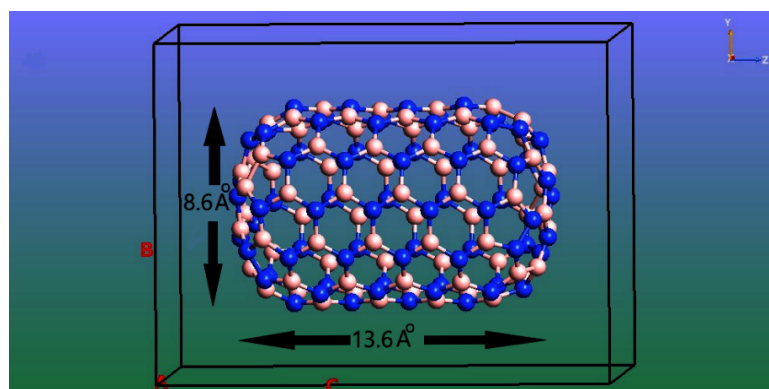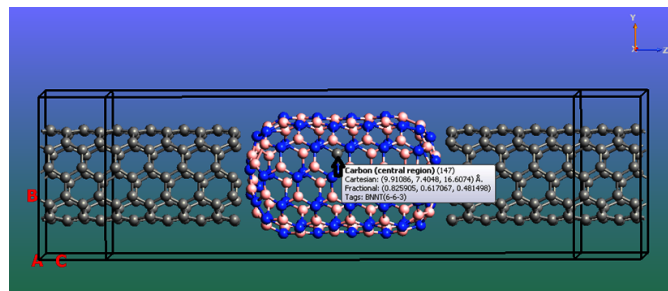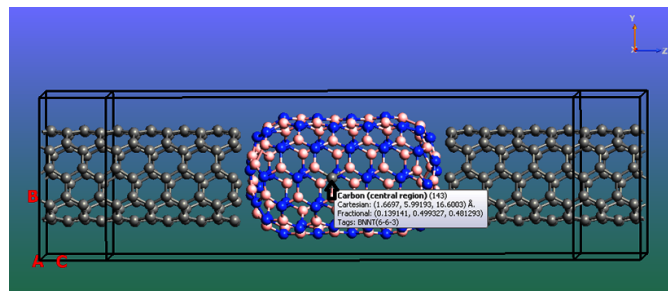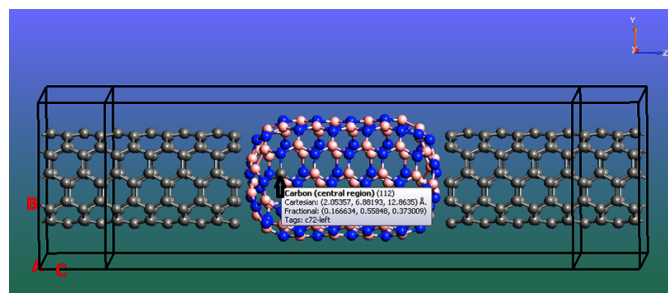

Figure 2. Two side-closed (6, 6) SWBNNT.

3a

3b

3c

3d

3e

3f

Figure 3. a) The tool created with $(6, 6)$ TSC-SWBNNT with C atom impurity rather than two $(5, 5)$ CNT electrodes on both sides and B atom in the center. b) The tool created with $(6, 6)$ TSC-SWBNNT with C atom impurity rather than two CNT electrodes $(5, 5)$ on both sides and N atom in the center. c) The tool created with $(6, 6)$ TSC-SWBNNT with C atom impurity rather than two $(5, 5)$ CNT electrodes on both sides and B atom on the left side. d) The tool formed with $(6, 6)$ TSC-SWBNNT with C atom impurity 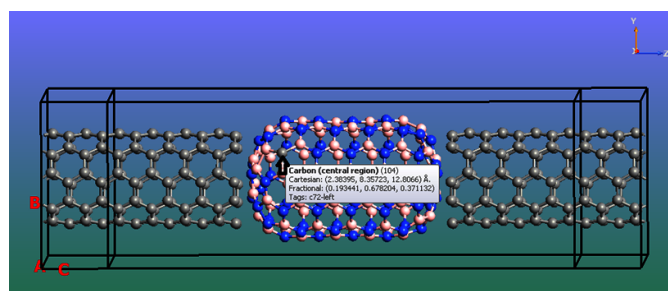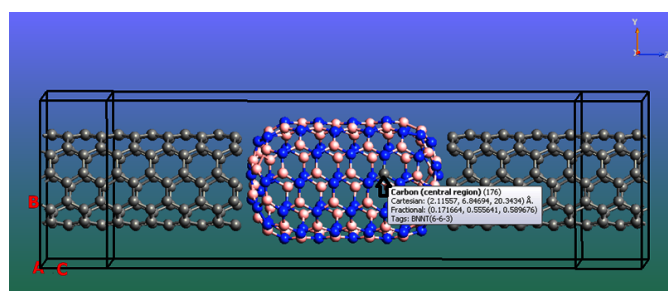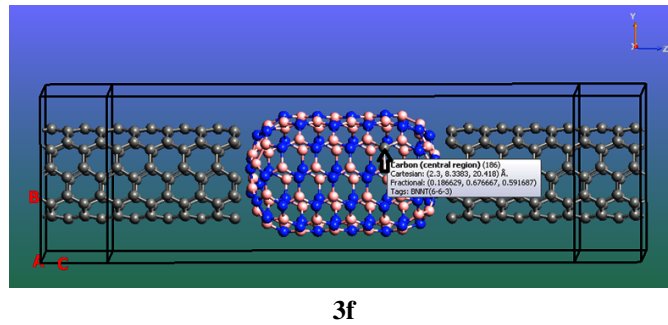rather than two $(5, 5)$ CNT electrodes on both sides and N atom on the left side. e) The tool generated with $(6, 6)$ TSC-SWBNNT with C atom impurity rather than two $(5, 5)$ CNT electrodes on both sides and B atom on the right side. f) Tool made with $(6, 6)$ TSC-SWBNNT with C atom impurity rather than two $(5, 5)$ CNT electrodes on both sides and N atom on the right side.

energy E, the transmission function $T(E, V)$ is:

$$T(E, V) = Tr \left[\Gamma_L(V) G^R(E, V) \Gamma_R(V) G^A(E, V) \right], \quad (1)$$

where, G^A and G^R are the advanced and retarded Green's functions of the central scattering area, respectively. $\Gamma_{LR} = i \left[\Sigma_{L(R)}^R(E) - \Sigma_{L(R)}^A(E) \right]$ shows the broadening function. Moreover, $\Sigma_{L(R)}^A(E)$ and $\Sigma_{L(R)}^R(E)$ represent the self-energies of the central scattering area, which includes all electrode effects [34, 35]. The system current is based on the Landauer-Butikker relationship:

$$I(V) = \frac{2e}{h} \int \left[f(E - \mu_L) - f(E - \mu_R) \right] T(E, V) dE. \quad (2)$$

where h is Planck's constant and e is the electron charge. Additionally, $f(E - \mu_{L(R)})$ and $\mu_{L(R)}$ represent the electron's Fermi distribution function in the left electrode (right) and the electrochemical potential of the left electrodes (right), respectively [36–38].

3. Results and discussion

Quantum ATK provides access to robust simulation tools to study systems, including semi-empirical tight binding, density functional theory, classical potentials, and non-equilibrium Green's functions (NEGF). The program was implemented, by creating the $(6, 6)$ TSC-SWBNNT device and optimizing and making the settings mentioned above. Figure 1 displays the tool constructed with pure $(6, 6)$ TSC-SWBNNT and two $(5, 5)$ CN electrodes on both sides. According to the figure, the total number of N and B atoms in $(6, 6)$ TSC-SUBNET equals 144. As seen in Figure 2, the $(6, 6)$ TSC-SWBNNT diameter is approximately 8.6 Å, and its length is about 13.6 Å. Both sides of the $(6, 6)$ TSC-SWBNNT are closed with N and B atoms of hexagonal and pentagonal structures. This $(6, 6)$ TSC-SWBNNT axis is parallel to the z-axis. Based on data in Figure 3a to Figure 3f, C atom was replaced with N and B atoms in the central (Figure 3a and Figure 3b), left (Figure 3c and

Figure 3d), and right (Figure 3e and Figure 3f) sections. Considering that the C atom possesses one electron more than the B atom, the C atom is substituted with the B atom, and one electron is inserted into the LUMO part of the $(6, 6)$ TSC-SWBNNT. Such impurity can make the $(6, 6)$ TSC-SWBNNT into an n-type semiconductor. In addition, the C atom possesses an electron less than the N atom; by substituting the C atom for the N atom, a hole is inserted into the HOMO part of the $(6, 6)$ TSC-SWBNNT, and this impurity can make the $(6, 6)$ TSC-SWBNNT into a p-type semiconductor [39, 40]. According to the periodic table of elements, C is more electronegative than B, and N is more electronegative than C, therefore, by optimizing the device, the location of the atoms changes. Replacing the C atom with each of the N and B atoms causes the bond length between the C atom and the surrounding atoms to change, and the bond length of the atoms further away from the C atom is also affected. Therefore, the two factors of creating an additional electron or hole and changing the bond length should be considered together. On the other hand, according to Eq. 1, the transmission coefficient is based on two factors, namely, the electronic energy of the molecule and the strength of the electrode/molecule coupling. Hence, changing the bond length and converting the nanotube to n or p type can affect the transmission coefficient.

A bias voltage from 0 to 5 volts has been used between the two right and left electrodes. The transmission spectrum within the energy range of -5 to 5 eV and with an accuracy of 0.1 eV has been drawn according to Figure 4a to Figure 4f for three values of bias voltage 0, 2.54, and 5 volts. Considering that in the   electronic transport process, electrons with Fermi energy play the most crucial role in establishing the current, we have demonstrated the transmission coefficients around the Fermi level. The right and left sides of the transmission spectrum figures are related to the effect of holes and electrons in the transmission spectrum, respectively. At the energy values of $+1.2$ and -1.8 eV, two peaks for the pure state can be detected in Figure 4a, indicating the possibility of tunneling at these

4a

4b

4c

4d

4e

4f
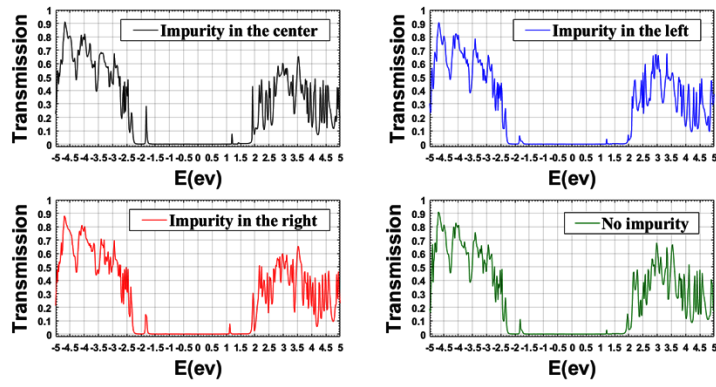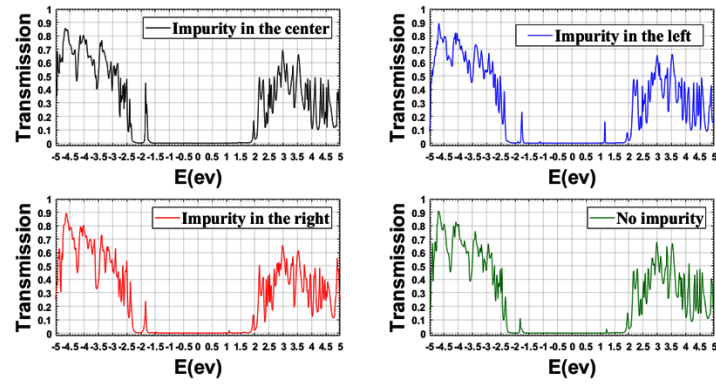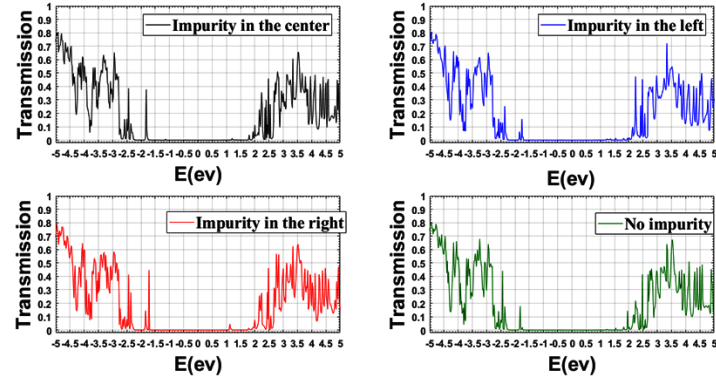
Figure 4. a) The transmission spectrum figure for $(6, 6)$ TSC-SWBNNT at 0 bias voltage in the pure state and impurity of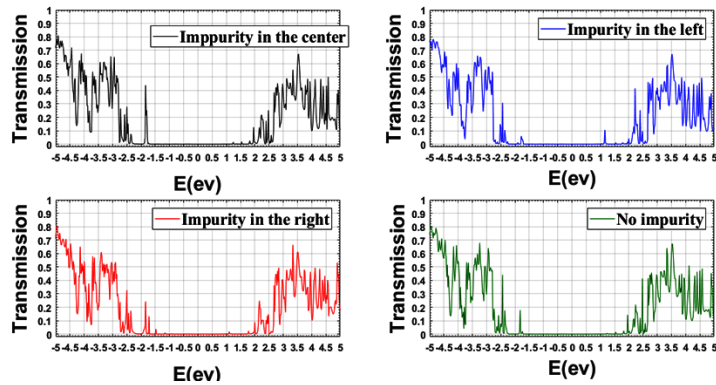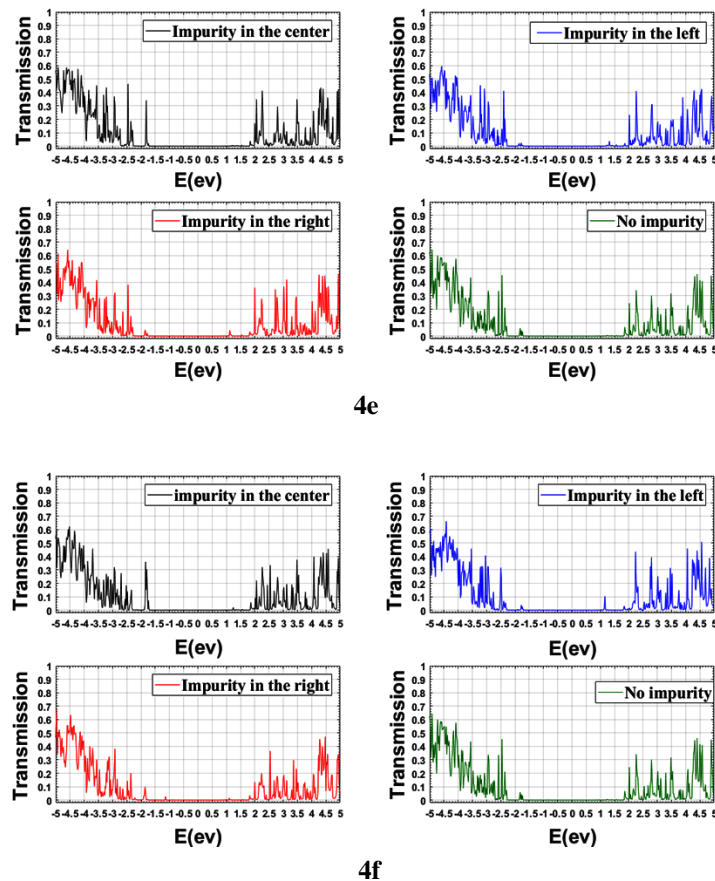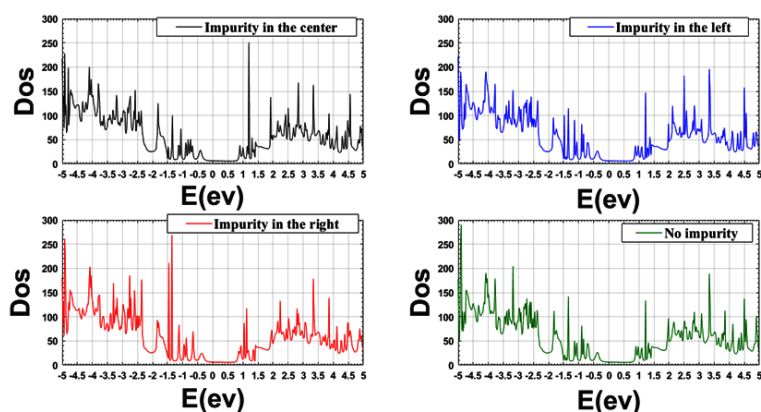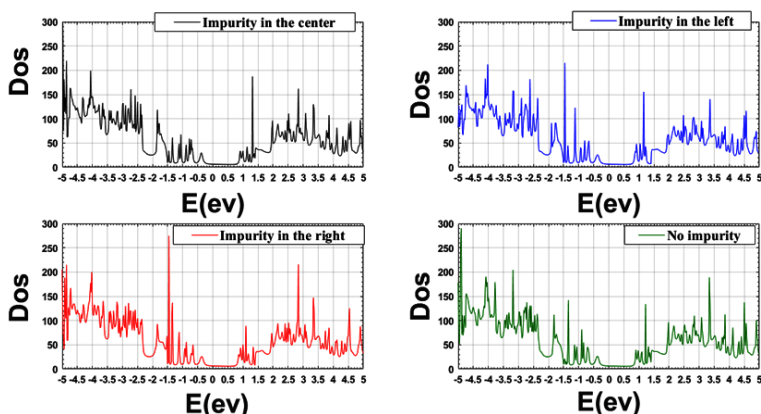 one C atom with one B atom in the three sections of the right, center, and left the nanotube. b) Transmission spectrum figure for $(6, 6)$ TSC-SWBNNT at 0 bias voltage in pure state and impurity of one C atom rather than one N atom in the three sections of the right, left, and center of the nanotube. c) The transmission spectrum figure for $(6, 6)$ TSC-SWBNNT at a bias voltage 2.5 V in the pure state and impurity of one C atom rather than one B atom in the three sections of the right, Left, and center of the nanotube. d) The transmission spectrum figure for $(6, 6)$ TSC-SWBNNT at a bias voltage of 2.5 V in the pure state and impurity of one C atom rather than one N atom in the three sections of the left, right, and center of the nanotube. e) The transmission spectrum figure for $(6, 6)$ TSC-SWBNNT at a bias voltage of 5 V in the pure state and impurity of one C atom rather than one B atom in the three sections of the left, right ,and center of the nanotube. f) The transmission spectrum figure for $(6, 6)$ TSC-SWBNNT at a bias voltage of 5 V in the pure state and impurity of one C atom instead of one N atom in the three sections of the left, right ,and center of the nanotube.

energy values. When the C atom replaces B or N, the height of transmission peaks increases and this indicates the increased transition probability at these points. According to Figure 4a to Figure 4f, the band gap from the left side is significantly reduced when the C atom is replaced by the N atom. Especially in the impurity state on the right side, the peak energy value decreases by 0.1 from 1.2 eV to 1.1 eV. A new hole is created when C is substituted by N, and the $(6, 6)$ TSC-SWBNNT becomes a p-type semiconductor. In addition, the number of holes increases in the capacity level, and the band gap decreases from the left side of the figure. When C impurity is substituted for B, the band gap slightly decreases from the right side of the figure. The reason is that when C is placed instead of B, the $(6, 6)$ TSC-SWBNNT confronts an increase in electrons and changes into an *n*-type semiconductor. Further, the number of the electrons in the conduction level is increases, At the same time, the band gap decreases from the right side of the fig-

ure. Of course, considering that by replacing C with B and N, the length of bonds changes in the different discussed states, the shape of the transmission spectrum curves also changes from the left and right sides. As the bias voltage increases, the height of the peaks decreases. In addition, the sharpness of the peaks of the curves in Figures **??**c and **??**d increased as the bias voltage increased to 2.5 V, while their width decreased slightly, indicating that the electrons and holes of the transmission spectrum were converted. This state of increasing the sharpness of the peaks at the bias voltage of 5 V can be observed in Figure 4e and Figure 4f. Furthermore, the height of the peaks in the left curves is higher than in the right, indicating a more significant influence of holes at negative energies than of electrons at positive energies. Moreover, by raising the bias voltage, the peaks height decreases, demonstrating more localization of holes and electrons with the increase of the bias voltage.
Figures 5a and Figure 5b illustrate the DOS for the $(6, 6)$

5a

5b

Figure 5. a) DOS figure for $(6,6)$ TSC-SWBNNT in pure state and impurity of one C atom rather than one B atom in the three sections of the left, right, and center of the nanotube. b) DOS figure for $(6,6)$ TSC-SWBNNT in pure state and impurity of one C atom in place of one N atom in the three sections of the left, right, and center of the nanotube.

TSC-SWBNNT in the pure and impurity states of one C atom in place of N and B atoms, respectively, in the left, right, and center of the nanotube. The DOS of a system describes the number of states available for occupation in each energy interval at each energy level [41, 42]. Based on the comparison of DOS figures and transmission spectrum figures, at energy points where resonance occurs between electrons hitting the molecular levels, the peaks of the transmission coefficient are close to the molecular levels, and the electron is transported, leading to conduction occurrence. According to Eq. 1, the transmission coefficient is based on the electronic energy of the molecule and the electrode/-molecule coupling strength. Thus, Green's function, the DOS of the coupled molecule, and the transition spectrum change as the electronic energy of the associated molecule represents a change. Hence, the large transmission functions values are close to the molecular levels of the $(6,6)$ TSC-SWBNNTs. In regular transport, it is assumed that the electron wave function spreads regularly throughout the system. Accordingly, when the electron's energy is approximately equal to the molecular alignment, a large transmission occurs, and the electron passes through the molecule resonantly.

Figure 6a and Figure 6b depict the current figure in terms of bias voltage. A bias voltage between of $0-5$ volts has been applied between the right and left electrodes. A threshold voltage is required to cause current to flow through the device, indicating that the device is in the off state at a low applied voltage. This is because there are no peaks in the Fermi energy range. The step-like behavior of the I-V figures can be explained by transmission coefficient curves (Figure 3a to Figure 3b). If $E_F = 0$ is considered, the length of the bias interval or the integral interval in the integral of the total current is actually $\left[-V_b/2, V_b/2\right]$. Moreover, the total current is the area under the transmission curve in the bias interval [Eq. 2]. The amount of current increases significantly when a new peak moves into the bias interval by increased bias voltage (opens a new channel). The current starts from the bias voltage of about 2.2 V, the amount of which is extremely low, up to about 3.5 volts. A significant jump in the current value can be observed for a bias voltage higher than 3.5 V. Replacing a C atom with a B atom and the creation of one more electron lead to the creation of an n-type semiconductor and an increase in the electron at the point of the presence of the C atom while a decrease in the passing current. Moreover, in the case of the substitution of a C atom instead of N, the current increases slightly with electron absorption, which is caused by the formation of one
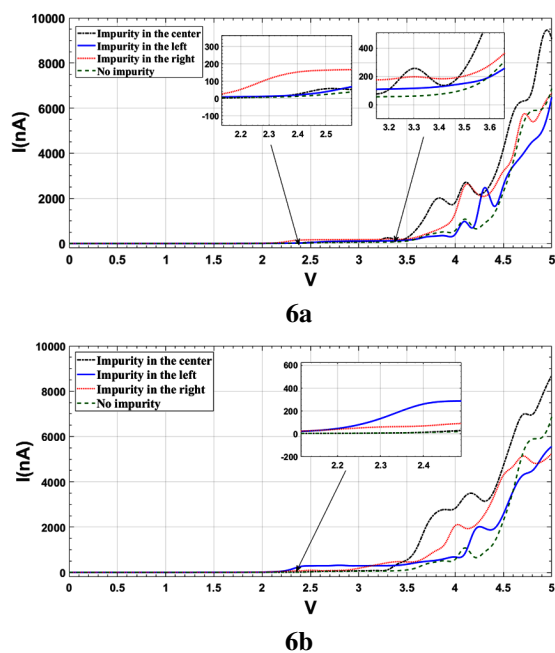
6a

6b

7a

7b

Figure 6. a) The current-voltage figure for $(6,6)$ TSC-SWBNNT pure and impurity state of one C atom instead of B atom in the three sections of the left, right, and center of the nanotube. b) The current-voltage figure for $(6,6)$ TSC-SWBNNT pure and impurity state of a C atom rather than an N atom in the three sections of the left, right, and center of the nanotube.

Figure 7. a) The dI/dV figure in terms of voltage for $(6,6)$ TSC-SWBNNT, pure and impurity state of a C atom instead of B atom in the three sections of the left, right, and center of the nanotube. b) The dI/dV figure in terms of voltage for $(6,6)$ TSC-SWBNNT pure and impurity state of a C atom rather than an N atom in the three sections of the left, right, and center of the nanotube.
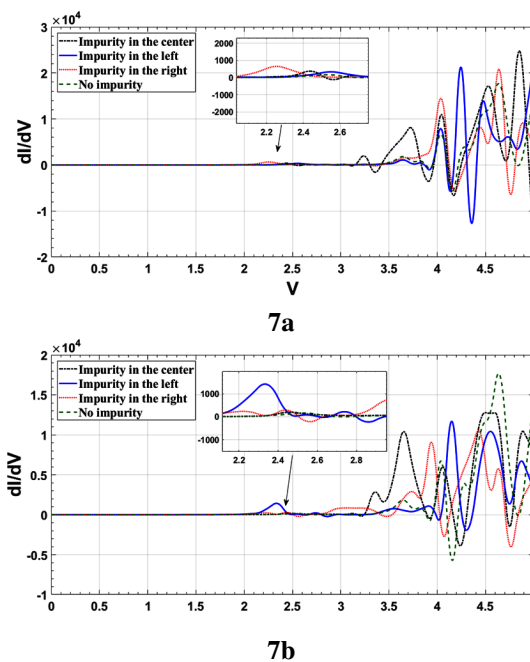
more hole in $(6,6)$ TSC-SWBNNT and creating a *p*-type semiconductor. On the other hand, the length of the bonds around the C atom changes by substituting the C atom with N and B. In the case of this nanotube, in almost all cases in the impurity state, the value of the passing current for various bias voltages is higher than the current in the pure state. As mentioned earlier, the replacement of the C atom rather than N and B, in addition to creating the semiconductors of *n*-type and *p*-type, respectively, the length of the bonds also changes, and changes in the length of the bonds increase the current in the impurity state compared to the pure state both for the substitution of C with B and for N. Additionally, due to the high density of holes and electrons in the two ends of the $(6,6)$ TSC-SWBNNT near the electrodes, as seen in Figure 6a and Figure 6b in the center of the $(6,6)$ TSC-SWBNNT, the amount of current increase is greater than the other two sides. In addition, in Figure 6a and Figure 6b, NDR can be detected for different bias voltages, which can be utilized as high-speed electronic switches in electrical circuits. The $(6,6)$ TSC-SWBNNT is not linked to the right and left electrodes, and electrons are only transported through tunneling. On the other hand,

given the asymmetric distribution of N and B atoms on both sides of the $(6,6)$ TSC-SWBNNT, due to the existence of pentagons close to the right and left electrodes (the number of N and B atoms in this pentagon is not equivalent) and the presence of the interference effect, NDR is observable in the current figure in terms of bias voltage.

Figure 7a and Figure 7b show the proportion of current differential/voltage differential for bias voltage from 0 to 5 V. Figure 7a and Figure 7b display system conduction as differential changes (dI/dV). The comparison of data in Figure 7a and Figure 7b indicates that, in general, the height of the peaks in Figure 7a is more significant that in Figure 7b; in other words, the conduction is more substantial in the case where C is placed instead of B. Figure 7a and Figure 7b illustrate that conduction has positive and negative values. Furthermore, in all curves, with the increase in voltage, there is a decrease in conductivity in some sections of the curves, representing that the curve has a negative slope, indicating NDR.

According to reference [23], Yadollahi *et al.* investigated the electronic transport properties of $(6,3)$ two side-closed SWBNNTs in pure and impurity states of C rather than

Table 1. Characteristics, diameter, and number of atoms of $(6,3)$ TSC-SWBNNTs and $(6,6)$ TSC-SWBNNTs structures.

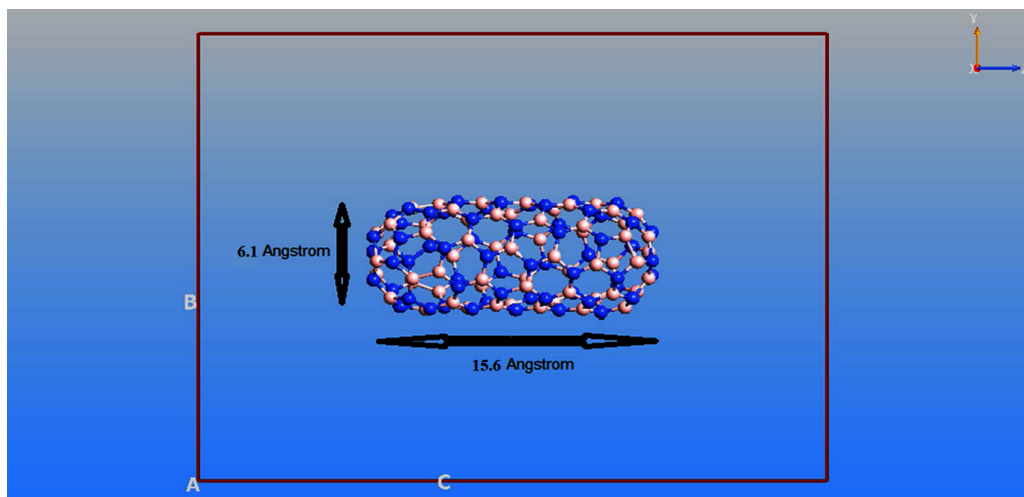| Structure	Length ($\mathring{A}$)	Diameter ($\mathring{A}$)	Atoms Number
$(6,3)$ TSC-SWBNNTs	15.6	6.1	120
$(6,6)$ TSC-SWBNNTs	13.6	8.6	144

Figure 8. Two side-closed $(6, 3)$ SWBNNT.

B and N atoms in different situations. Figure 8 shows the structure of the $(6, 3)$ two side-closed SWBNNT. This structure contains $N = 120$ N and B atoms, the nanotube length is 15.6 Å, and its diameter is 6.1 Å. Furthermore, in this work, the differences in the transport properties of $(6, 6)$ two side-closed SWCNTs were also examined in compared to the $(6, 3)$ two side-closed SWBNNTs. The investigation of transmission spectra at bias voltages of 0, 2.5, and 5 volts, both in pure and impurity states of C in place of N and B atoms in the right, left, and central positions of the nanotube, reveals that the number of peaks and their heights in the $(6, 6)$ SWBNNT structure is higher than the $(6, 3)$ SWBNNT structure at the same voltages. This difference can be attributed to the number of atoms in the $(6, 6)$ SWBNNT structure and the effect of the nanotube geometrical features, such as its length and diameter (see Table 1). On the other hand, the comparison of the current passing through the $(6, 3)$ SWBNNT and $(6, 6)$ SWBNNT structures reveals that the current passing through the $(6, 6)$ SWBNNT structure is more significant than that through the $(6, 6)$ SWBNNT structure in both in pure and impurity state of C instead of N and B atoms in right, left, and central

positions. For instance, at a voltage of 5 volts, the current for the $(6, 6)$ SWBNNT and $(6, 3)$ SWBNNT structures at the center, with C instead of B, is 9.03×10^3 nA and 2.62×10^3 nA, respectively, and with C instead of N, it is 8.69×10^3 nA and 4.24×10^3 nA, respectively (see Table 2).

Therefore, the summary of the investigations for these two structures indicates that the transmission spectra, peak heights, and current passing through the $(6, 6)$ SWBNNT structure are greater than those of the $(6, 3)$ SWBNNT structure, in both pure and impurity conditions. According to Table 1, the results show that the length of the $(6, 6)$ SWBNNT structure is smaller, and its diameter is larger than the $(6, 3)$ SWBNNT structure. Since conductivity is directly proportional to the length and inversely proportional to the diameter hence, it is expected that the conductivity in the structure of $(6, 6)$ SWBNNT is higher than that of $(6, 3)$ SWBNNT, and the current through it is also increased, which agrees with the results.

Table 2. Electric current values at 5 V voltage for structures $(6, 6)$ TSC-SWBNNTs and $(6, 3)$ TSC-SWBNNTs.

Stracture			Voltage ($5V$) and Current (nA)
	No Impurity or Impurity	No Impurity	2.62×10^3
	Impurity Carbon instead Boron	Center	2.51×10^3
		Left	5.14×10^3
$(6, 3)$ TSC-SWBNNTs		Right	5.85×10^3
	Impurity Carbon instead Nitrogen	Center	4.24×10^3
		Left	1.99×10^3
		Right	7.64×10^3
	No Impurity or Impurity	No Impurity	6.86×10^3
	Impurity Carbon instead Boron	Center	9.03×10^3
		Left	6.48×10^3
$(6, 6)$ TSC-SWBNNTs		Right	6.66×10^3
	Impurity Carbon instead Nitrogen	Center	8.69×10^3
		Left	5.56×10^3
		Right	5.25×10^3

4. Conclusion

In this paper, the impurity of a single C atom was investigated considering N and B atoms in the right, left, and center on the electronic properties of the $(6, 6)$ TSC-SWBNNT. With the impurity of a single C atom, the transmission spectrum figure is changed, and the band gap is influenced and represents a slight reduction. The band gap was investigated in $(6, 6)$ TSC-SWBNNTs structures in pure and impurity states. In addition, the DOS was plotted and compared with the shape of the transmission spectrum, and it was also shown that at energies where resonance occurs, tunneling of electrons, holes, and changes in the current value can be observed. Finally, the presence of NDR in current figures in terms of bias voltage can be used as an advantage in the production of high-speed electronic switch devices.

Ethical Approval
This manuscript does not report on or involve the use of any animal or human data or tissue. So the ethical approval is not applicable.

Funding
No funding was received to assist with conducting this study and the preparation of this manuscript.

Authors Contributions
All authors have contributed equally to prepare the paper.

Availability of Data and Materials
The data that support the findings of this study are available from the corresponding author upon reasonable request.

Conflict of Interests
The authors declare that they have no known competing financial interests or personal relationships that could have appeared to influence the work reported in this paper.

Open Access
This article is licensed under a Creative Commons Attribution 4.0 International License, which permits use, sharing, adaptation, distribution and reproduction in any medium or format, as long as you give appropriate credit to the original author(s) and the source, provide a link to the Creative Commons license, and indicate if changes were made. The images or other third party material in this article are included in the article's Creative Commons license, unless indicated otherwise in a credit line to the material. If material is not included in the article's Creative Commons license and your intended use is not permitted by statutory regulation or exceeds the permitted use, you will need to obtain permission directly from the OICCPress publisher. To view a copy of this license, visit https://creativecommons.org/licenses/by/4.0.

References

[1] Ahmet Engin Pazarçeviren Zafer Evis Turhan, Emine Ayşe and Ayşen Tezcaner. "Properties and applications of boron nitride nanotubes". *Nanotechnology*, **33(24)**:242001, 2022. DOI: https://doi.org/10.1001/jamaoncol.2019.1460.

[2] R.L. Siegel, K.D. Miller, H.E. Fuchs, and A. Jemal. Cancer statistics, CA. *Cancer J. Clin*, 72:7–33, 2022. DOI: https://doi.org/10.3322/caac.21708.

[3] D.L. Hill, D.J. Hawkes, M.J. Gleeson, T.C. Cox, A.J. Strong, W.L. Wong, and A. Sofat. Accurate frameless registration of MR and CT images of the head: Applications in planning surgery and radiation therapy. *Radiol*, **191**:447–454, 1994. DOI: https://doi.org/10.1021/acs.jpclett.0c00143.

[4] X. Gu, D.D. Li, G.H. Yeoh, R.A. Taylor, and V. Timchenko. Heat generation in single magnetic nanoparticles under near-infrared irradiation. *J. Phys. Chem. Lett*, **11**:2182–2187, 2020. DOI: https://doi.org/10.1021/acs.jpclett.0c00143.

[5] Z. Shen, J. Song, Z. Zhou, B.C. Yung, M.A. Aronova, Y. Li, Y. Dai, W. Fan, Y. Liu, Z. Li, H. Ruan, R.D. Leapman, L. Lin, G. Niu, X. Chen, and A. Wu. Dotted core–shell nanoparticles for T_1-weighted MRI of tumors. *Adv. Mater*, **30**:e1803163, 2018. DOI: https://doi.org/10.1002/adma.201803163.

[6] J.S. Ananta, B. Godin, R. Sethi, L. Moriggi, X. Liu, R.E. Serda, R. Krishnamurthy, R. Muthupillai, R.D. Bolskar, L. Helm, M. Ferrari, L.J. Wilson, and P. Decuzzi. Geometrical confinement of gadolinium-based contrast agents in nanoporous particles enhances T_1 contrast. *Nat. Nanotechnol*, **5**:815–821, 2010. DOI: https://doi.org/10.1038/nnano.2010.203.

[7] J.A. Sherwood, M.C. Rich, K. Lovas, J.M. Warram, M.S. Bolding, and Y. Bao. T_1-enhanced MRI-visible nanoclusters for imaging-guided drug delivery. *Nanoscale*, **9**:11785–11792, 2017.

[8] Y. Sun, H.S. Kim, S. Kang, Y.J. Piao, S. Jon, and W.K. Moon. Magnetic resonance imaging-guided drug delivery to breast cancer stem-like cells. *Adv. Healthc. Mater*, **7**:e1800266, 2018. DOI: https://doi.org/10.1002/adhm.201800266.

[9] H. Struyfs, D.M. Sima, M. Wittens, A. Ribbens, N. Pedrosa de Barros, T.V. Phan, M.I. Ferraz Meyer, L. Claes, E. Niemantsverdriet, S. Engelborghs, W. Van Hecke, and D. Smeets. Automated MRI volumetry as a diagnostic tool for

Alzheimer's disease: Validation of icobrain dm. *Neuroimage Clin*, **26**:102243–102247, 2020. DOI: https://doi.org/10.1016/j.nicl.2020.102243.

[10] K. Liu, L. Dong, Y. Xu, X. Yan, F. Li, Y. Lu, W. Tao, H. Peng, Y. Wu, Y. Su, D. Ling, T. He, H. Qian, and S. Yu. Stable gadolinium based nanoscale lyophilized injection for enhanced MR angiography with efficient renal clearance. *Biomater*, **158**:74–85, 2018. DOI: https://doi.org/10.1016/j.biomaterials.2017.12.023.

[11] D. Ni, Z. Shen, J. Zhang, C. Zhang, R. Wu, J. Liu, and W. Bu. Integrating anatomic and functional dual-mode magnetic resonance imaging: design and applicability of a bifunctional contrast agent. *ACS Nano*, **10**:3783–3790, 2016. DOI: https://doi.org/10.1021/acsnano.6b00462.

[12] G. Huang, H. Li, J. Chen, Z. Zhao, L. Yang, X. Chi, Z. Chen, X. Wang, and J. Gao. Tunable T_1 and T_2 contrast abilities of manganese-engineered iron oxide nanoparticles through size control. *Nanoscale*, **17**:10404–10412, 2014. DOI: https://doi.org/10.1039/c4nr02680b.

[13] P. Mi, D. Kokuryo, H. Cabral, H. Wu, Y. Terada, T. Saga, and K. Kataoka. A pH-activatable nanoparticle with signal-amplification capabilities for non-invasive imaging of tumour malignancy. *Nat. Nanotechnol*, **11**:724–730, 2016. DOI: https://doi.org/10.1038/nnano.2016.72.

[14] H. Zhou, M. Guo, J. Li, F. Qin, Y. Wang, T. Liu, and Y. Liu. Hypoxia-triggered self-assembly of ultrasmall iron oxide nanoparticles to amplify the imaging signal of a tumor. *J. Am. Chem. Soc*, **143**:1846–1853, 2021. DOI: https://doi.org/10.1021/jacs.0c10245.

[15] Z. Han, X. Wu, S. Roelle, C. Chen, W.P. Schiemann, and Z. Lu. Targeted gadofullerene for sensitive magnetic resonance imaging and risk-stratification of breast cancer. *Nat. Commun*, **8**:692–697, 2017. DOI: https://doi.org/10.1038/s41467-017-00741-y.

[16] X. Li, S. Lu, Z. Xiong, Y. Hu, D. Ma, W. Lou, C. Peng, M. Shen, and X. Shi. Light-addressable nanoclusters of ultrasmall iron oxide nanoparticles for enhanced and dynamic magnetic resonance imaging of arthritis. *Adv. Sci*, **6**:1901800, 2019. DOI: https://doi.org/10.1002/advs.201901800.

[17] D. Cohen, R. Mashiach, L. Houben, A. Galisova, Y. Addadi, D. Kain, and A. Bar-Shir. Glyconanofluorides as immunotracers with a tunable core composition for sensitive hotspot magnetic resonance imaging of inflammatory activity. *ACS Nano*, **15**:7563–7574, 2021. DOI: https://doi.org/10.1021/acsnano.1c01040.

[18] J. Wahsner, E.M. Gale, A. Rodríguez-Rodríguez, and P. Caravan. Chemistry of MRI contrast agents: Current challenges and new frontiers. *Chem. Rev*, **119**:957–1057, 2019. DOI: https://doi.org/10.1021/acs.chemrev.8b00363.

[19] Y. Xiao, R. Paudel, J. Liu, C. Ma, Z. Zhang, and S. Zhou. MRI contrast agents: Classification and application (Review). *Int. J. Mol. Med*, **38**:1319–1326, 2016. DOI: https://doi.org/10.3892/ijmm.2016.2744.

[20] K.M. Hasebroock and N.J. Serkova. Toxicity of MRI and CT contrast agents. *Expert Opin. Drug Metab. Toxicol*, **5**:403–416, 2009. DOI: https://doi.org/10.1517/17425250902873796.

[21] S. Rasaneh, H. Rajabi, and F. Johari Daha. Activity estimation in radioimmunotherapy using magnetic nanoparticles. *Chin. J. Cancer Res*, **27**:203–208, 2015. DOI: https://doi.org/10.3978/j.issn.1000-9604.2015.03.06.

[22] S. Rasaneh, H. Rajabi, M.H. Babaei, and S. Akhlaghpoor. MRI contrast agent for molecular imaging of the HER2/neu receptor using targeted magnetic nanoparticles. *J. Nanopart. Res*, **13**:2285–2293, 2011. DOI: https://doi.org/10.1007/s11051-010-9991-5.

[23] H. Rajabi, S. Rasaneh, and S. Salehi. Synthesis and biological evaluation of 99mTc-Chitosan nanoparticles as a potential radiopharmaceutical for liver imaging. *Synth. React. Inorg. Met*, **46**:1450–1454, 2016. DOI: https://doi.org/10.1080/15533174.2015.1137010.

[24] S. Rasaneh and M. Dadras. The possibility of using magnetic nanoparticles to increase the therapeutic efficiency of herceptin antibody. *Biomed. Eng-Biomed. Tech.*, **60**:485–490, 2015. DOI: https://doi.org/10.1515/bmt-2014-0192.

[25] B. Sadeghi. One-Pot synthesis of Ag/Fe_3O_4 nanocomposite: Preparation and characterization. *Adv. Mater. Process*, **5**:82–92, 2009. URL https://api.semanticscholar.org/CorpusID:55006948.

[26] A. Szpak, S. Fiejdasz, W. Prendota, T. Straczek, C. Kapusta, J.S. Szmyd, M. Nowakowska, and S. Zapotoczny. T_1–T_2 dual-modal MRI contrast agents based on superparamagnetic iron oxide nanoparticles with surface attached gadolinium complexes. *J. Nanoparticle Res*, **16**:1–11, 2014. DOI: https://doi.org/10.1007/s11051-014-2678-6.

[27] A. Amraee, Z. Alamzadeh, R. Irajirad, A. Sarikhani, H. Ghaznavi, H. Ghadiri Harvani, S. Rabi Mahdavi, S. Shirvalilou, and S. Khoei. Theranostic RGD@Fe3O4-Au/Gd NPs for the targeted radiotherapy and MR imaging of breast cancer. *Cancer Nanotechnol*, **14**:1–20, 2023. DOI: https://doi.org/10.1186/s12645-023-00214-6.

[28] V.P. Torchilin. Recent advances with liposomes as pharmaceutical carriers. *Nat. Rev. Drug Discov*, **4**:145–160, 2005. DOI: https://doi.org/10.1038/nrd1632.

[29] V.J. Venditto and F.C. Szoka. Cancer nanomedicines: So many papers and so few drugs! *Adv. Drug Deliv. Rev*, **65**:80–88, 2013. DOI: https://doi.org/10.1016/j.addr.2012.09.038.

[30] Y. Matsumura and H. Maeda. A new concept for macromolecular therapeutics in cancer chemotherapy: Mechanism of tumoritropic accumulation of proteins and the antitumor agent smancs. *Expert Opin. Drug Metab. Toxicol*, **46**:6387–92, 1986. URL https://api.semanticscholar.org/CorpusID:7103917.

[31] A.A. Lozano-Pérez, A.L. Gil, S.A. Pérez, N. Cutillas, H. Meyer, M. Pedreño, and J. Ruiz. Antitumor properties of platinum (iv) prodrug-loaded silk fibroin nanoparticles. *Dalton Trans*, **44**:13513–13521, 2015. DOI: https://doi.org/10.1039/c5dt00378d.

[32] L.D. Leserman, J.N. Weinstein, R. Blumenthal, and W.D. Terry. Receptor-mediated endocytosis of antibody-opsonized liposomes by tumor cells. *Proc. Natl. Acad. Sci. U. S. A.*, **77**:4089–4093, 1980. DOI: https://doi.org/10.1073/pnas.77.7.4089.

[33] N. Kamaly, Z. Xiao, P.M. Valencia, A.F. Radovic-Moreno, and O.C. Farokhzad. Targeted polymeric therapeutic nanoparticles: Design, development and clinical translation. *Chem. Soc. Rev*, **41**:2971–3010, 2012. DOI: https://doi.org/10.1039/c2cs15344k.

[34] A. Koshkaryev, R. Sawant, M. Deshpande, and V. Torchilin. Immunoconjugates and long circulating systems: Origins, current state of the art and future directions. *Adv. Drug Deliv. Rev*, **65**:24–35, 2013. DOI: https://doi.org/10.1016/j.addr.2012.08.009.

[35] J. Schnorr, S. Wagner, C. Abramjuk, I. Wojner, T. Schink, T. J. Kroencke, E. Schellenberger, B. Hamm, H. Pilgrimm, and M. Taupitz. Comparison of the iron oxide-based blood-pool contrast medium VSOP-C184 with gadopentetate dimeglumine for first-pass magnetic resonance angiography of the aorta and renal arteries in pigs. *Invest. Radiol*, **39**:546–553, 2004. DOI: https://doi.org/10.1097/01.rli.0000133944.30119.cc.

[36] B.H. Kim, N. Lee, H. Kim, K. An, Y.I. Park, Y. Choi, K. Shin, Y. Lee, S.G. Kwon, H.B. Na, J. Park, T. Ahn, Y.W. Kim, W.K. Moon, S.H. Choi, and T. Hyeon. Large-scale synthesis of uniform and extremely small-sized iron oxide nanoparticles for high-resolution T_1 magnetic resonance imaging contrast agents. *J. Am. Chem. Soc*, **133**:12624–12631, 2011. DOI: https://doi.org/10.1021/ja203340u.

[37] E.A. Park, W. Lee, Y.H. So, Y.S. Lee, B.S. Jeon, K.S. Choi, E.G. Kim, and W.J. Myeong. Extremely small pseudoparamagnetic Iron Oxide nanoparticle as a novel blood pool T_1 magnetic resonance contrast agent for 3 T whole-heart coronary angiography in canines: Comparison with gadoterate meglumine. *Invest. Radiol*, **52**:128–133, 2017. DOI: https://doi.org/10.1097/RLI.000000000000321.

[38] Y. Rui, B. Liang, F. Hu, J. Xu, Y. Peng, P. Yin, Y. Duan, C. Zhang, and H. Gu. Ultra-large-scale production of ultrasmall superparamagnetic iron oxide nanoparticles for T1-weighted MRI. *RSC Adv*, **6**:22575–22585, 2016. DOI: https://doi.org/10.1039/C6RA00347H.

[39] Z. Shen, T. Chen, X. Ma, W. Ren, Z. Zhou, G. Zhu, A. Zhang, Y. Liu, J. Song, Z. Li, H. Ruan, W. Fan, L. Lin, J. Munasinghe, X. Chen, and A. Wu. Multifunctional theranostic nanoparticles based on exceedingly small magnetic iron oxide nanoparticles for T_1-weighted magnetic resonance imaging and chemotherapy. *ACS nano*, **11**:10992–11004, 2017. DOI: https://doi.org/10.1021/acsnano.7b04924.

[40] T. Vangijzegem, D. Stanicki, S. Boutry, Q. Paternoster, L. Vander Elst, R.N. Muller, and S. Laurent. VSION as high field MRI T_1 contrast agent: Evidence of their potential as positive contrast agent for magnetic resonance angiography. *Nanotechnol*, **29**:265103, 2018. DOI: https://doi.org/10.1088/1361-6528/aabbd0.

[41] M. Wagner, S. Wagner, J. Schnorr, E. Schellenberger, D. Kivelitz, L. Krug, M. Dewey, M. Laule, B. Hamm, and M. Taupitz. Coronary MR angiography using citrate-coated very small superparamagnetic iron oxide particles as blood-pool contrast agent: Initial experience in humans. *J. Magn. Reson. Imaging*, **34**:816–823, 2011. DOI: https://doi.org/10.1002/jmri.22683.

[42] H. Wei, O.T. Bruns, M.G. Kaul, E.C. Hansen, M. Barch, A. Wiśniowska, O. Chen, Y. Chen, N. Li, S. Okada, J.M. Cordero, M. Heine, C.T. Farrar, D.M. Montana, G. Adam, H. Ittrich, A. Jasanoff, P. Nielsen, and M.G. Bawendi. Exceedingly small iron oxide nanoparticles as positive MRI contrast agents. *Proc. Natl. Acad. Sci. U.S.A.*, **114**:2325–2330, 2017. DOI: https://doi.org/10.1073/pnas.1620145114.